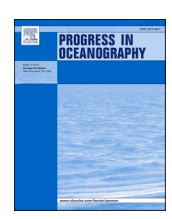
ELSEVIER

Contents lists available at ScienceDirect

Progress in Oceanography

journal homepage: www.elsevier.com/locate/pocean



Circulation and cross-shelf exchanges in the Malvinas Islands Shelf region

Elbio D. Palma^{a,*}, Ricardo P. Matano^b, Vincent Combes^b

- a Departamento de Física, Universidad Nacional del Sur e Instituto Argentino de Oceanografía (CONICET), Bahía Blanca, Argentina
- ^b College of Earth, Ocean, and Atmospheric Sciences, Oregon State University, Corvallis, Oregon, USA

ARTICLE INFO

Keywords:
South Atlantic Ocean
Malvinas Islands
Cross-shelf exchanges
Obduction mechanisms
Ocean modelling
Oceanographic connectivity

ABSTRACT

The Malvinas Islands Shelf (MIS) encompasses one of the most productive portions of the southwestern Atlantic. Large phytoplankton blooms, which constitute the base of the marine food web, emerge from the northern sector of the MIS and extend hundreds of kilometers northward along the Patagonian shelfbreak. The physical processes contributing to MIS fertilization are poorly understood. Here we use the results of a high-resolution ocean model to characterize circulation and water mass exchanges between the MIS and the Southern Ocean, as well as to identify the physical processes underlying fertilization of the shelf waters. Model results show that the shelf is characterized by an anticyclonic circulation pattern in the southwestern region that intensifies during summer and weakens during winter. The blocking effect of the islands leads to development of an upwind westwardflowing current in the northern portion of the MIS, recirculation cells in the western portion, and a northward throughflow in the narrow strait separating them. Particle tracking experiments reveal that the northern portion of the Drake Passage is the largest water mass source for the MIS. Passive tracers indicate that the place where the Antarctic Circumpolar Current collides with the MIS is the main site for the outcropping of deep waters. Subsequent outcropping is largely driven by the synergetic interaction of tides and wind forcing. After spreading along the southwestern shelfbreak, the concentration of tracer peaks in the winter and decays during the spring. In summer, the tracer accumulates on the lee of the islands in agreement with satellite images of chlorophyll-a concentration. Additional experiments show that there is an important contribution of MIS waters to the Patagonian shelfbreak front.

1. Introduction

The Malvinas Islands archipelago is located at the southern end of the Patagonian Shelf (PS) (51°S – 53°S, Fig. 1a). It comprises more than two hundred islands, but two of them, Gran Malvina and Soledad, which are separated by the narrow San Carlos Strait, stand out because of their size (Fig. 1b). The Malvinas Islands are bounded on the deep ocean side (z > 200 m) by a swift branch of the Antarctic Circumpolar Current (ACC), whose downstream continuation is known as the Malvinas Current.

For the present purposes we define the Malvinas Islands Shelf (MIS) as the portion of the PS shown in Fig. 1b. Its northwestern corner is connected to the PS but it is otherwise surrounded by deep ocean waters. The MIS is one of the most productive portions of the southwestern Atlantic (Boltovskoy, 2000; Marrari et al., 2017), being a feeding and spawning ground for squid, toothfish, cod, herring and numerous birds and mammals species (Agnew et al., 2000; Arkhipkin et al., 2004; Ashford et al., 2012). This rich marine ecosystem is sustained by intense

blooms of chlorophyll-a, which extend towards the similarly productive shelfbreak region (Romero et al., 2006; Painter et al., 2010, Fig. 1a). The physical mechanisms sustaining MIS productivity are unknown. It has been suggested that this productivity is associated with shelfbreak upwelling, but analytical and numerical models indicate that the impact of this phenomenon is largely restricted to the shelfbreak region (Matano and Palma, 2008; Miller et al., 2011; Combes and Matano, 2018). Instead, the MIS blooms appear to be related to local, yet unidentified, physical processes. The MIS is also a potentially important oil and gas reservoir (Richards and Hillier, 2000; Zabanbark, 2011; Jones et al., 2019). Petroleum related activities—including production, offshore drilling and transit of tankers—generate environmental risks that cannot be assessed without proper information about the regional oceanic circulation. Such information is necessary for the management of the local marine ecosystem because oil and fishing industries operate in important areas of reproductive aggregations and foraging grounds of many marine birds and mammals (Baylis et al., 2019). Therefore, a quantitative knowledge and dynamical understanding of the three-dimensional

E-mail address: uspalma@criba.edu.ar (E.D. Palma).

 $^{^{\}ast}$ Corresponding author.

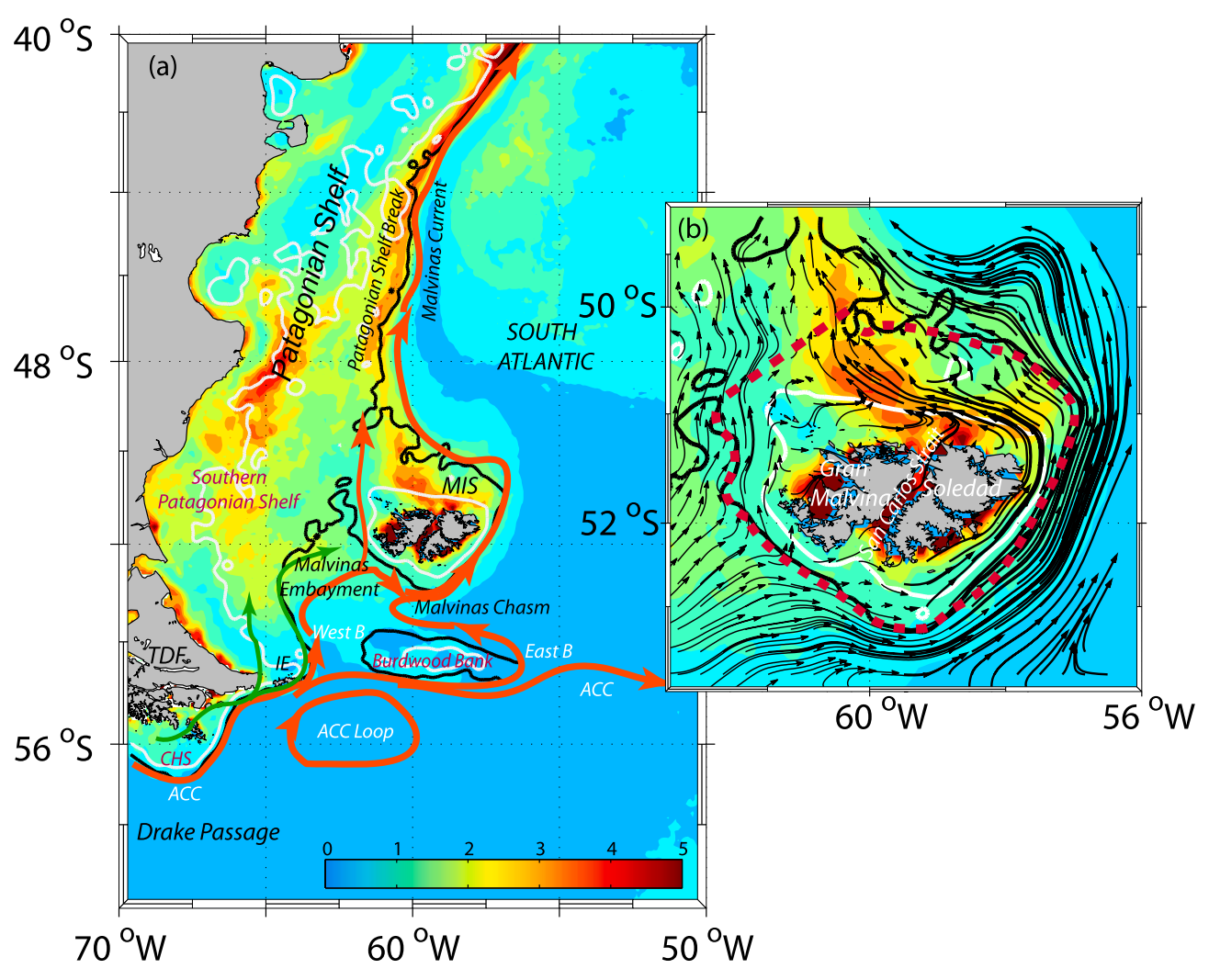


Fig. 1. Geographical setting (a) Model domain showing satellite surface chlorophyll-a concentration (mg/m^3) derived from MODIS 2003–2018 January climatology over the Patagonian Shelf. Spatial resolution is 9 km \times 9 km. The white and black lines indicate the 100 m and 200 m isobaths respectively. Orange curved lines indicate the approximate direction of the deep ocean flow. ACC: Antarctic Circumpolar Current, West B: west branch of the ACC, East B: east branch of the ACC. Green lines are representative of shelf inflow into the Patagonian Shelf. CHS: Cape Horn Shelf, TDF: Tierra del Fuego, IE: Isla de los Estados. (b) Inset showing chlorophyll-a concentration and the annual-mean depth-mean circulation obtained from the model. The dashed red line delineates a polygon covering the approximate limit of the Malvinas Islands Shelf (MIS). (For interpretation of the references to color in this figure legend, the reader is referred to the web version of this article.)

MIS circulation is not only of physical interest, but also of biological and environmental importance for this region.

There is scant information about the oceanic circulation over the MIS. Circulation in the deep ocean region surrounding the MIS has been described from hydrographic observations (Zyranov and Severov, 1979; Piola and Gordon, 1989; Guerrero et al., 1999, Frey et al, 2021) and high-resolution numerical models (Fetter and Matano, 2008; Combes and Matano, 2018; Matano et al., 2019; Guihou et al., 2020, Artana et al, 2021) (Fig. 1a). Observation based descriptions of the MIS circulation are far more scarce and based on few synoptic hydrographic observations (e.g., Arkhipkin et al., 2004; Arkhipkin et al., 2010). Here we use a suite of model simulations to characterize the circulation over the MIS and identify the physical processes underlying its rich marine ecosystem including its connection to the deep ocean region.

2. Model description

Our analysis is based on the results of a regional model that extends from 58° to 38° S and from 69° to 51° W with $1/24^\circ$ degree horizontal resolution and 40 sigma levels in the vertical, with higher vertical

 Table 1

 Characteristics of the numerical experiments described in the text. Sfluxes = Surface fluxes, Bfluxes = Open Boundary fluxes.

	Initial Stratification	Forcing	Obs
CTRL	WOA	Tides, Winds, Sfluxes & Bfluxes	Seasonal surface and boundary forcing
ACC&TIDES	44	Tides, Sfluxes & Bfluxes	No Winds
ACC&WINDS	"	Winds, Sfluxes & Bfluxes	No Tides
ACC_ONLY	"	Sfluxes & Bfluxes	No tides or winds
TIDES_ONLY	T & S constant	Tides, no Sfluxes or Bfluxes	Barotropic, no winds

resolution at the top and bottom layers (Fig. 1a) (Matano et al., 2019; Palma et al., 2020). The bottom topography is derived from the ETOPO1 (1' resolution) (Amante and Eakins, 2009), which is smoothed to minimize pressure gradient errors associated with terrain-following coordinates.

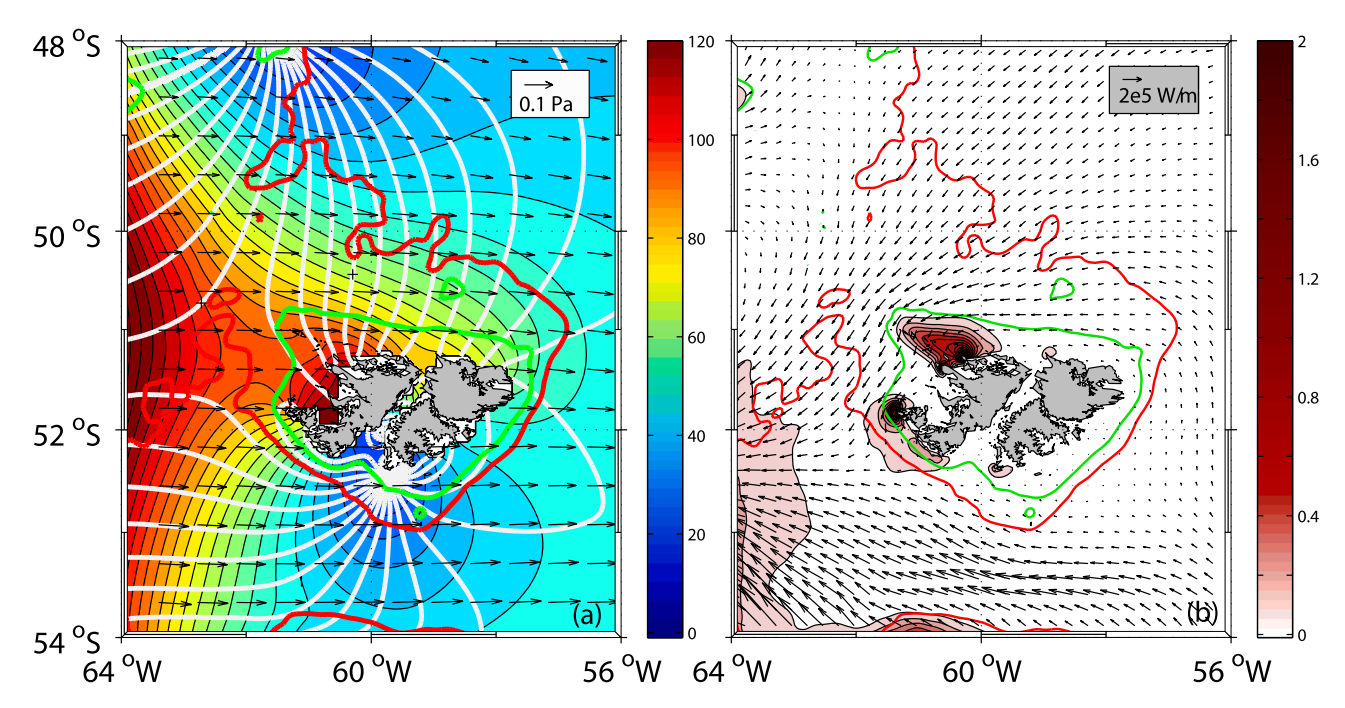


Fig. 2. (a) Tidal regime around Malvinas Islands derived from the model results. (a) tidal amplitude (colours in cm, contour interval CI: 5) and cotidal lines (white in degrees, CI: 10). (b) tidal dissipation (colour in W/m^2) and energy flux (vectors in W/m). The annual mean wind stress vectors are indicated as black arrows in panel (a). The red and green thick lines indicate the 200 m and 100 m isobaths respectively. (For interpretation of the references to color in this figure legend, the reader is referred to the web version of this article.)

A combination of radiation and advection conditions are used at the open boundaries (Marchesiello, et al., 2001). In the most realistic experiment (CTRL) the model is forced with amplitudes and phases of the M2 tide interpolated from a global TPXO6 tidal model (Egbert et al., 1994) and with climatological values of temperature, salinity and velocity fields extracted from a regional model of the entire Southwestern Atlantic region at 1/12° horizontal resolution (Combes and Matano, 2014a, CM14 model hereafter). A barotropic simulation forced with global tides (Table 1) shows that the tidal cycle over the MIS is dominated by the M2 semidiurnal component, which propagates counterclockwise around the islands (Fig. 2a). Tidal amplitudes are higher than 1.4 m near Gran Malvina island (~51°S) and decay towards the amphidromic point located in the south. Tidal energy flows westward in the northern and southern portions of the MIS converging in the southern PS, a region of large tidal amplitudes. A small portion of this energy is dissipated to the northwest and southwest of Gran Malvina island (Fig. 2b). Model results are in agreement with previous simulations (Glorioso and Flather, 1997, Palma et al., 2004).

At the surface, the model is forced with the mean climatological wind stress derived from the 1999-2012 Quikscat-ASCAT climatology and heat and freshwater fluxes derived from the Comprehensive Ocean-Atmosphere Data Set (COADS) (Da Silva et al., 1994). The annual mean wind stress distribution over the MIS is characterized by a band of strong westerlies that intensify during late fall and early winter (Fig. 2a). The heat flux also includes a tendency-restoring term to the SST climatology derived from the CM14 model following the procedure described in Barnier (1998). Vertical mixing is parameterized with a K-Profile Parameterization (KPP) scheme (Large et al., 1994) and bottom friction follows a quadratic formulation. There is no explicit horizontal mixing included in the model simulations. Further description of the CM14 model, including comparison with in-situ and satellite observations, is presented in Combes and Matano (2014a; 2014b; 2018), Matano et al. (2014) and Strub et al. (2015). Results of the current model as applied to the Burdwood Bank circulation and the Gulf of San Jorge region are given in Matano et al. (2019) and Palma et al. (2020).

The CTRL experiment is initialized with the January climatology of

the World Ocean Atlas (WOA09; Locarnini et al., 2010; Antonov et al., 2010) and integrated for five years. The model fields from the last year are used for analysis of the circulation. Sensitivity experiments identify the contribution of different forcing mechanisms (ACC, local winds and tides) to MIS circulation (Table 1). Experiments using passive tracers and floats allows to characterize the connection between the MIS and its surrounding region.

3. Results

3.1. Mean circulation and cross-shelf exchanges.

A detailed description of the circulation patterns produced by our CTRL experiment in the deep-ocean region, including comparison with observations, can be found in Matano et al. (2019). For the sake of completeness, we include a brief description here. In the Drake Passage the circulation is dominated by the northern jet of the ACC. The inshore portion of this jet, here defined by the 200 m and 1000 m isobaths, transports surface and Antarctic Intermediate Waters (AAIW) to the tip of Isla de los Estados, whereupon it bifurcates and surrounds the Burdwood Bank (Fig. 1a). The narrow and shallow channel (~500 m deep) to the west of the bank allows the passage of a lighter type of AAIW [27.05 $<\sigma_{\theta}$ (potential density) < 27.10, Guerrero et al., 1999] while the deeper (>1800 m) and wider channel to the east is also the entry point for a heavier type of AAIW [27.10 $< \sigma_{\theta} <$ 27.20, Piola and Gordon, 1989]. The eastward branch describes an abrupt cyclonic loop closely following the bathymetry of the Malvinas Chasm. The western branch turns eastward inside the Malvinas Embayment, roughly following the 300 m isobath, impinging on the MIS continental slope close to 51°.5S, 61°W. After collision, the main portion of this branch continues as a strong eastward flowing jet while the remainder leaks to the north. Both ACC branches rejoined near the MIS southern slope and, with additional contributions, become part of the Malvinas Current (Fig. 1a). The circulation patterns produced by the model are quite similar to those inferred from hydrographic observations (Piola and Gordon, 1989), current estimates supported by direct velocity measurements and

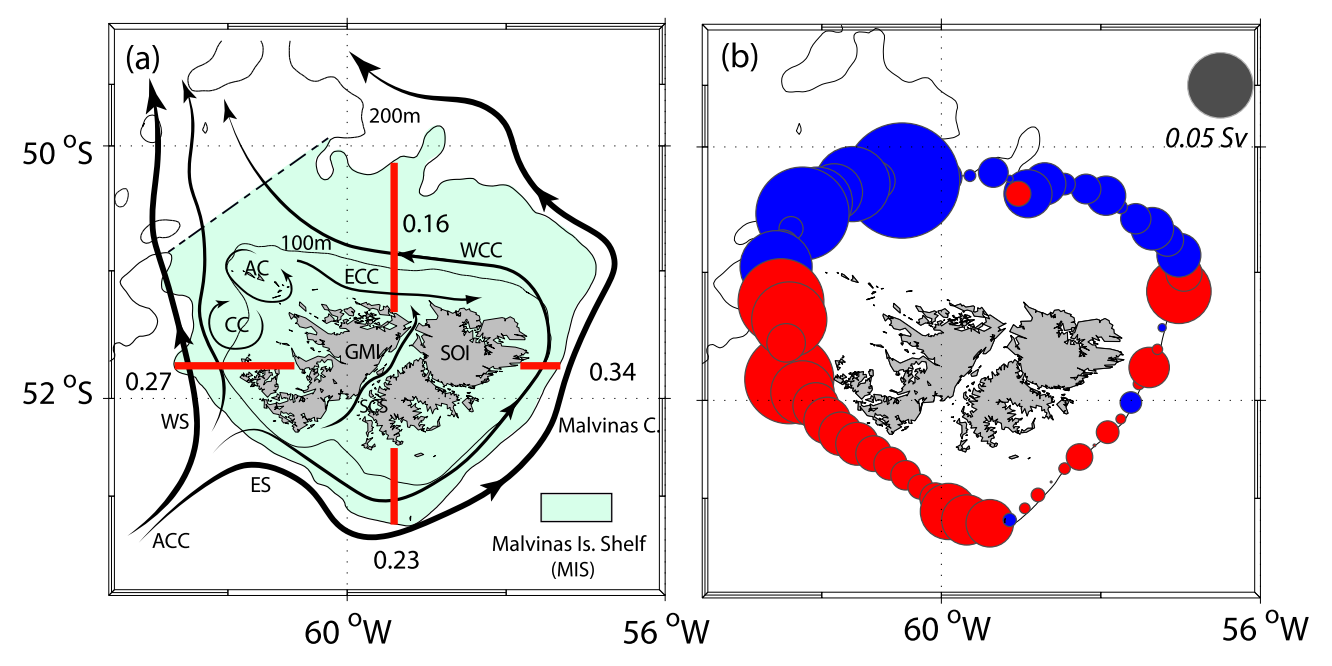


Fig. 3. (a) Schematic ocean circulation around the Malvinas Islands Shelf. Thick black lines indicate flow offshore the 200 m isobath (WS: Western stream; ES: Eastern stream), thin black lines are flow between the 200 and 100 m isobaths (WCC: Westward Counter Current, ECC: Eastward Coastal Current; AC: Anticyclonic recirculating cell; CC: Cyclonic cell). Numbers indicate shelf transport (Sv) at the selected cross-sections. The grey lines indicate the 200 m and 100 m isobaths respectively. GMI: Gran Malvina Island, SOI: Soledad Island, SCS: San Carlos Strait. (b) Cross-shelf exchanges. Red circles represent inflows and blue circles outflow; the size of each circle is proportional to the magnitude of the exchange. (For interpretation of the references to color in this figure legend, the reader is referred to the web version of this article.)

satellite altimetric data (Frey et al, 2021; see also Suppl. Fig. S1) and model reanalysis products (Artana et al, 2021).

The circulation over the outer portion of the MIS (100–200 m isobaths) mimics the offshore flow, with currents that wrap around the sides of the islands thus leading to the development of an anticyclonic circulation pattern in the southwestern sector (Fig. 1b). The presence of the islands generates an eastward flowing coastal current, and an offshore westward current flowing along the 100 isobath against the eastward winds in the northern portion of the MIS. The islands also lead

to the development of recirculation cells in the western sector of the shelf and a northern throughflow in the narrow strait separating the two largest islands (Fig. 3a). The annual mean volume transport around the MIS varies between a maximum of $0.34~\rm Sv$ in the east and a minimum of $0.16~\rm Sv$ in the north.

To determine the origin and fate of the MIS waters we compute the cross-shelf transports along the MIS perimeter, which include the portion of the shelfbreak (here defined by the 200 m isobath) surrounding the islands and the northward section closing the MIS polygon

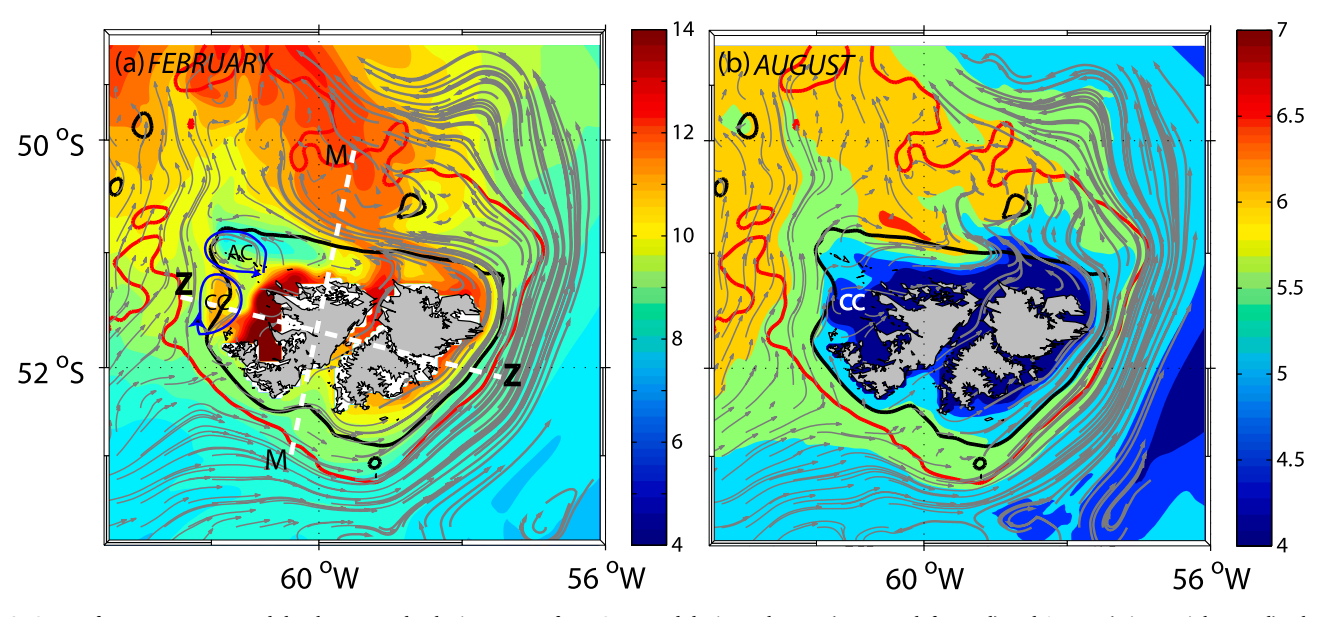


Fig. 4. Sea surface temperature and depth-averaged velocity vectors from CTRL and during February (summer, left panel) and August (winter, right panel). The red and black thick lines indicate the 200 m and 100 m isobaths respectively. AC: Anticyclonic cell, CC: Cyclonic cell. Z-Z indicates the direction of a zonal cross-section. M-M is the direction of a meridional cross-section. Note the different color scale for the summer and winter panels. (For interpretation of the references to color in this figure legend, the reader is referred to the web version of this article.)

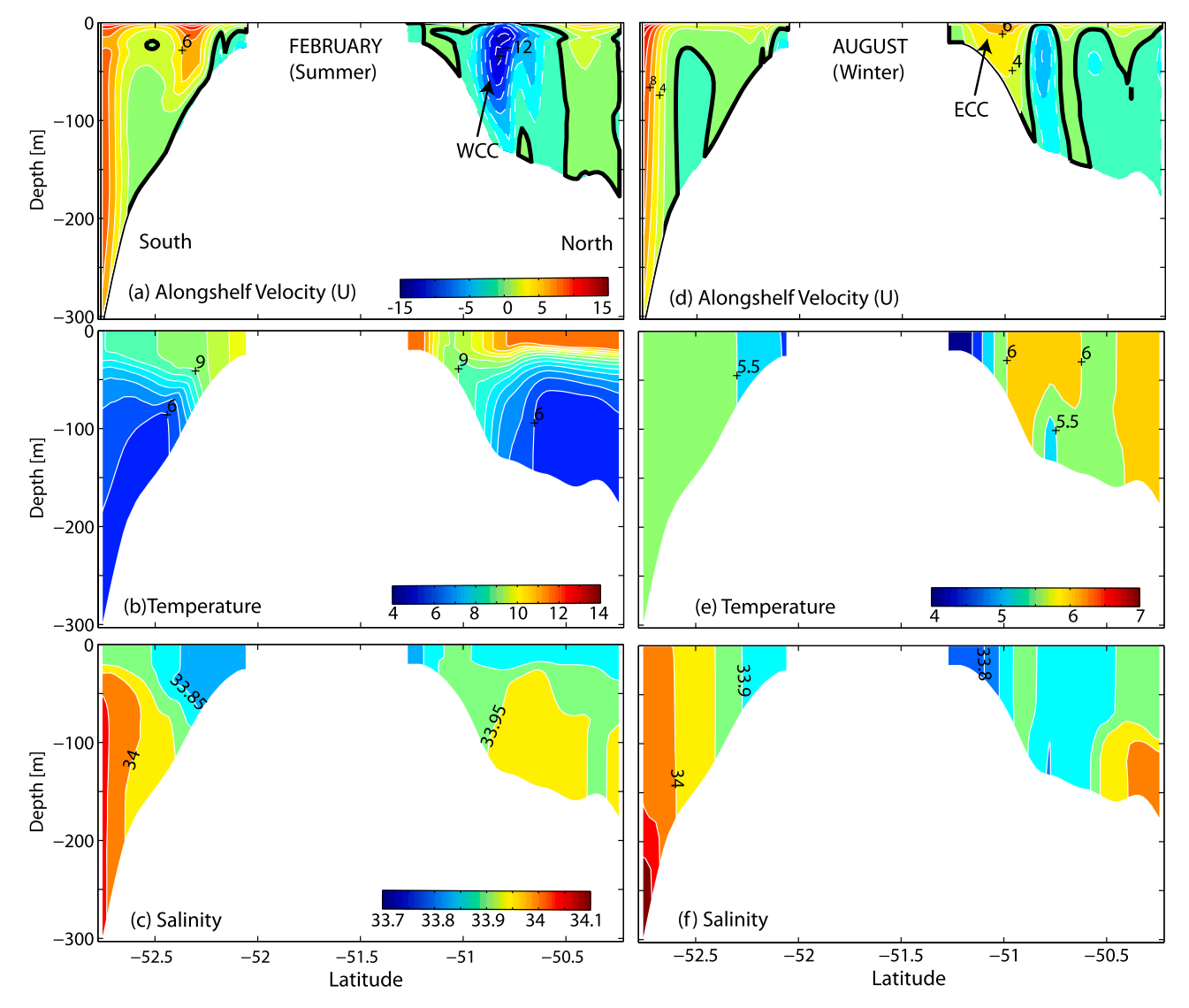


Fig. 5. (a,d) Alongshelf velocity, (b,e) temperature, and (c,f) salinity at the meridional cross-section M-M (see Fig. 4a). Left panels are from February, right panels from August. Note the different color scale for the summer and winter panels.

(Fig. 3b). Inflows are largely concentrated in the southwestern region and outflows in the northwest. The largest inflow is observed in the region where the northern branch of the ACC collides with the MIS (Fig. 3a). Ancillary analysis indicates that at this location, upwelling in the bottom boundary layer is largely driven by topographic steering and, to a lesser extent, by the bottom stress curl. Cross-shelf exchanges are sharply reduced on the eastern side, although they are still significant in the southeastern corner due to an abrupt change of the shelfbreak orientation. Outflows are larger in the northwestern section connecting the MIS to the PS and diminished towards the east where they are entrained into the Malvinas Current.

3.2. Seasonal variability

Previous studies have shown that the alongshelf transport over the PS strengthens during fall and weakens during spring (Palma et al., 2008; Combes and Matano, 2014a). Combes and Matano (2018) concluded that these seasonal variations are driven by the synergetic interaction between the onshore fluxes of mass drawn from the Drake Passage (remote forcing) and the local (over the shelf) wind stress forcing. The complementary analysis presented herein focuses on the particulars of the seasonal variations of the circulation over the MIS.

Seasonal variations in the CTRL experiment are relatively small and largely constrained to changes of flow intensity, with only small modifications of the time mean circulation patterns (Fig. 1b and Fig. 4). The broad anticyclonic system over the eastern side of the MIS intensifies during summer and weakens during winter (Fig. 4). Volume transport changes are only significant in the northern section, where the eastward coastal current and westward countercurrent surrounding the islands are seasonally out of phase: in summer/winter the stronger westward current strengthens/weakens while the eastward current weakens/ strengthens (Fig. 5a and d). Correspondingly, the mean (westward) along-shelf transport in the northern region (from the coast to the 200 m isobath) increases during summer and peaks in fall (~0.35 Sv), after which it weakens during winter decaying to almost zero in early spring (September). These results are in agreement with those reported by Combes and Matano (2018) using a lower resolution model. Two recirculation cells of opposing polarity develop during the summer (Fig. 3a and Fig. 4a). During winter, the cyclonic cell moves inshore and the anticyclonic cell disappears while the flow in the eastern portion of the northern shelf is deflected towards the north, thus augmenting the detrainment of shelf waters (Fig. 4b).

Shallow thermoclines and haloclines develop during summer and disappear during winter. Summer thermoclines are stronger in the

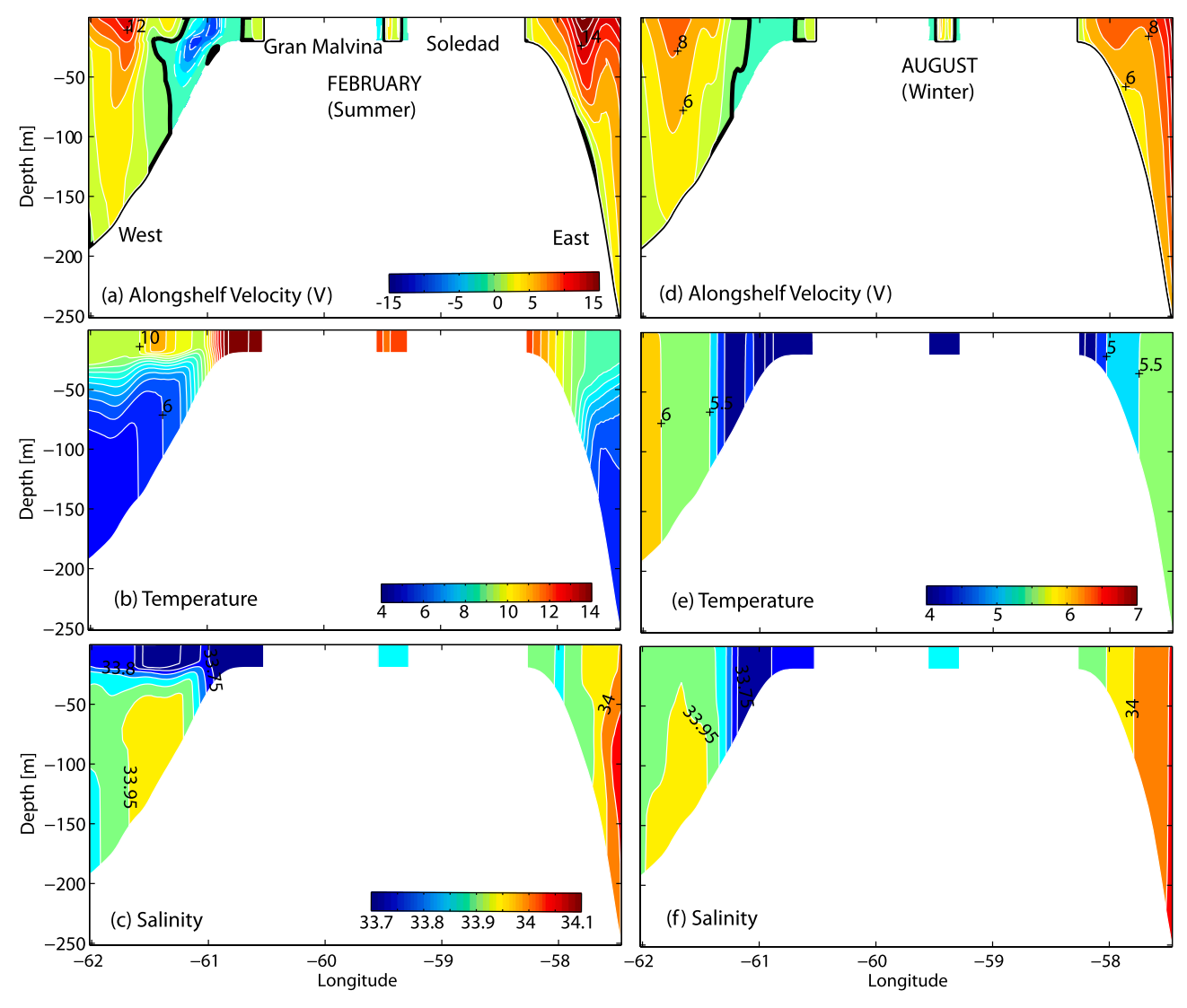


Fig. 6. (a,d) Alongshelf velocity, (b,e) temperature, and (c,f) salinity at the zonal cross-section Z-Z (see Fig. 4a). Left panels are from February, left panels from August. Note the different color scale for the summer and winter panels.

northern (~25 m depth, Fig. 5b) and western (~40 m depth, Fig. 6b) regions, deepening towards the coast in the southeastern downwelling areas. There is no significant density stratification over the shallow portions of the MIS (z < 50 m), but there are strong horizontal gradients associated with the development of thermohaline fronts. These fronts encircle regions of relatively warmer waters during summer and colder waters during winter (Fig. 4). Westerly winds lead to upwellingfavorable conditions to the north of the main islands and downwelling favorable conditions in the south. Thus, during summer, surface fronts are more intense in the northern region. In the south, these fronts are stronger in the bottom layer and below 50 m (Fig. 5b). Due to the orientation of the islands, the wind has an alongshore, upwelling inducing component along the western coast of Gran Malvina and downwelling in the eastern coast of Soledad (Fig. 6b). Warmer waters are found in the western region, particularly along the inner shelf (z < 50 m) of Gran Malvina (Fig. 4a), where tidal mixing homogenizes the water column (Fig. 2a and Fig. 6b). Offshore temperatures are colder due to the intrusion of the western limb of the ACC, especially near the anticyclonic recirculating cell located at the northwestern corner (Fig. 4a). Salinity stratification during summer reflects intrusions of saltier sub-Antarctic Mode Water (SAMW, S > 33.95), particularly in the northern (Fig. 5c) and western sectors (Fig. 6c) of the MIS. Winter is characterized by a vertical homogenization of the water column and a

strong cooling of the inner shelf with the possible formation of SAMW (Guerrero et al., 1999) (Fig. 5 and Fig. 6, right panels).

3.3. Source of MIS waters

Marine ecosystems are highly dependent on their physical connections to nearby and faraway regions. Determination of these connections is particularly germane to the regulation of the fisheries industry, which requires the protection of fishing as well as spawning grounds. Patagonian toothfish, for example, is a commercially important species that is captured over the MIS but whose spawning grounds are largely unknown (Ashford et al., 2012; Lee et al., 2018; Harte, 2020; Randhawa et al., manuscript submitted). To identify water mass sources and connectivity patterns we did a backward in time integration of the trajectories of 117,348 particles over the MIS using the model 3D velocity field. Particles are initially located within the MIS polygon, distributed at 5 m separation throughout the water column and released at monthly intervals (19,558 particles/month). The integration is carried out over a 180-day period, after which we identify the origins of the particles reaching the MIS. Fig. 7 shows the density of particles at the end of the numerical integration (180 days before reaching the MIS). Concentration density represents the area-averaged number of particles inside each model cell, final values are expressed as a percentage of their initial

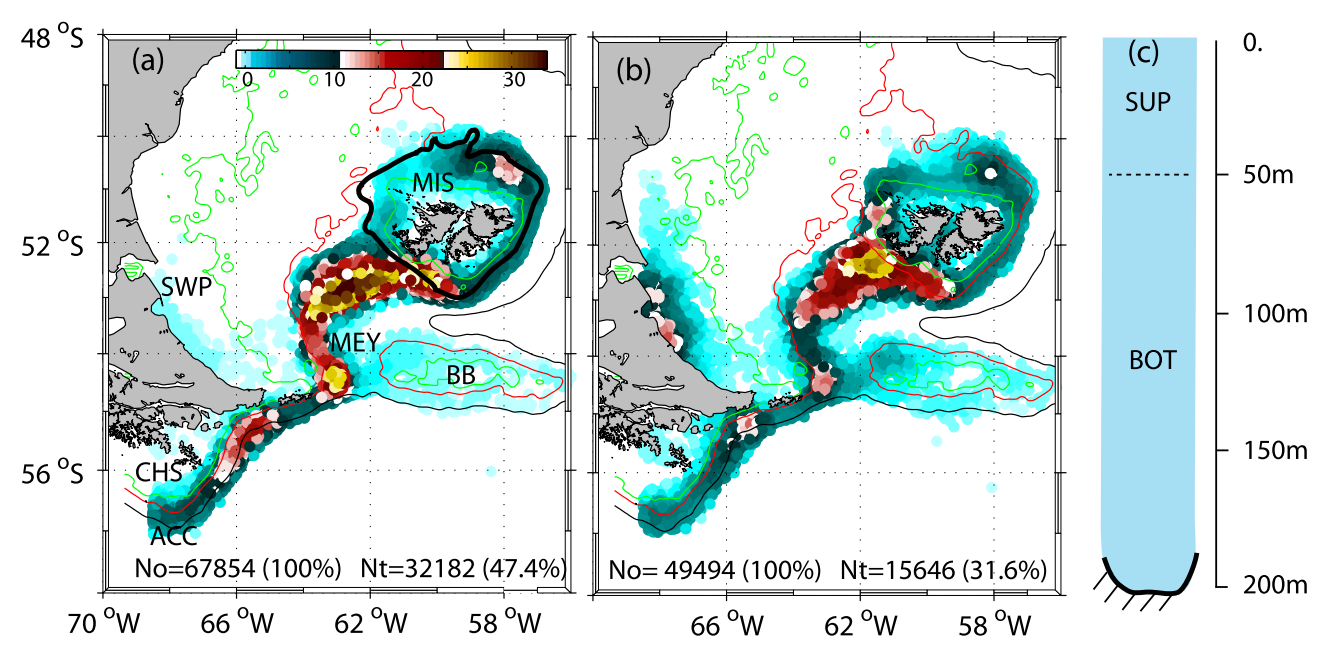


Fig. 7. Backward tracking experiment. Particle concentration (scatter plot) 180 days before reaching the MIS scaled with respect to its initial value (%). (a) particles released over the MIS polygon (thick black line in panel a) and between 50 m and the bottom (BOT, panel c), (b) particles released between 0 and 50 m (SUP). The 100 m (green), 200 m (red) and 1000 m (black) isobaths are indicated. No = initial number of particles over the MIS, Nt = final number of particles inside the domain at day 180. ACC: Antarctic Circumpolar Current, CHS: Cape Horn Shelf, MEY: Malvinas Embayment, BB: Burdwood Bank, SWP: Southwestern Patagonian shelf. (For interpretation of the references to color in this figure legend, the reader is referred to the web version of this article.)

concentration. We distinguish between particles released in the deep layer (67,854 particles from $z=50\,\text{m}$ to bottom, Fig. 7a) and the surface layer (49,494 particles from z=0 to $z=50\,\text{m}$, Fig. 7b). The dispersal patterns of all particles extends towards the Malvinas Embayment, whereupon they follow the 200 m isobath towards the outer portion of the Cape Horn shelf and into the northern jet of the ACC. Most particle trajectories can be traced back to the Cape Horn shelf and to the northern branch of the ACC. A smaller, but still significant, number of particles from the surface layer originate in the coastal areas of southern Patagonia and the Burdwood Bank (Fig. 7, right panel). A census at the end of time integration shows that 53% of the deep layer particles (~35,600) and 68% of the surface layer particles (~33,800) cross the 69°W longitude line.

To complement the prior analysis we did an online, forward in time particle tracking diagnostic using CTRL. This approach allows a better representation of the effect of high-frequency processes such as tides and turbulent mixing on particles' trajectories. In this diagnostic 14,000 particles are released within four different regions on the ACC, the Cape Horn shelf, southwestern Patagonia and the Burdwood Bank. The polygons encircling these regions are marked in their respective panels in Fig. 8. ACC polygons are located between the 200 m and 400 m isobaths, the remaining polygons circumscribe shelf domains (z < 200 m). For the ACC polygon two different release levels are considered: one above (upper portion) and one below 200 m (lower portion). To characterize seasonal variations associated with the time of release the diagnostics are repeated with an additional particle release at the beginning of each season: December (summer), March (autumn), June (winter) and September (spring). After a 360-day integration the connection between source regions and the MIS is graded by the number of particles linking them. The final census considers the number of particles reaching the surface (0–50 m) and deep layers (50 m-bottom) of the MIS. Results are summarized in Table 2a and Fig. 8.

The upper portion of the ACC polygon (z $<200\,$ m) is the most important source for the MIS waters during all seasons, $\sim\!43\%$ of the particles released in this region reach the MIS on annual average. During summer, more ACC particles reach the deep layer (z >50 m) of the MIS. During spring particles originated in the ACC are more homogeneously

distributed throughout the MIS water column. The spring uplift of particles occurs within the Malvinas Embayment (Fig. 8a). During summer, the uplift is inhibited by the stronger stratification of the deep ocean waters (not shown). The Cape Horn shelf is the second largest contributor of MIS waters (~36% of the released particles), particularly to the MIS surface layer (z < 50 m) in spring. Most of these waters originate in the outer portion of the Cape Horn shelf (offshore the 100 m isobath), and are upwelled after crossing the eastern tip of Tierra del Fuego and Isla de los Estados (Fig. 8b). During winter there is a significant contribution (>34%) of Cape Horn particles to the deeper portions (z > 50 m) of the MIS (Table 2a). This increase is related to a larger subduction rate promoted by winter convection. There is a weak connection between the Burdwood Bank and the MIS—as measured by the number of particles trajectories connecting both regions— which strengthens during summer and fall (~15%) (Table 2a and Fig. 8c). The coastal portion (inshore the 100 m isobath, SWP polygon) of Tierra del Fuego makes an additional contribution (~18%). Most of these particles are locally upwelled by tidal and wind forcing and advected towards the MIS surface layer (Fig. 8d).

Additional particles are released in the lower portion (z > 200 m) of the ACC and the offbank region of the Burdwood Bank polygons (200 m to 400 m isobaths). Between 10 and 20 % of the ACC particles reach the MIS, with an average transit time of 165 days. Very few particles released in the deep ocean region surrounding the Burdwood Bank reach the MIS (<1%); most of them are entrained in the Malvinas Current and advected northward (not shown). Only those obducted to the top of the bank are transported to the MIS by the surface circulation in late spring and summer (Fig. 8c). Detailed analysis of the Burdwood Bank circulation indicates that during this period most of the Burdwood Bank waters are flushed out towards the northwest (Matano et al., 2019).

3.4. Residence times

We also use particle tracking to estimate residence time, which is defined as the time that it takes to evacuate 63% of particles (*e*-folding time) from the MIS. To estimate seasonal variations of residence time we make a particle release (45,000 particles) during each month of the last

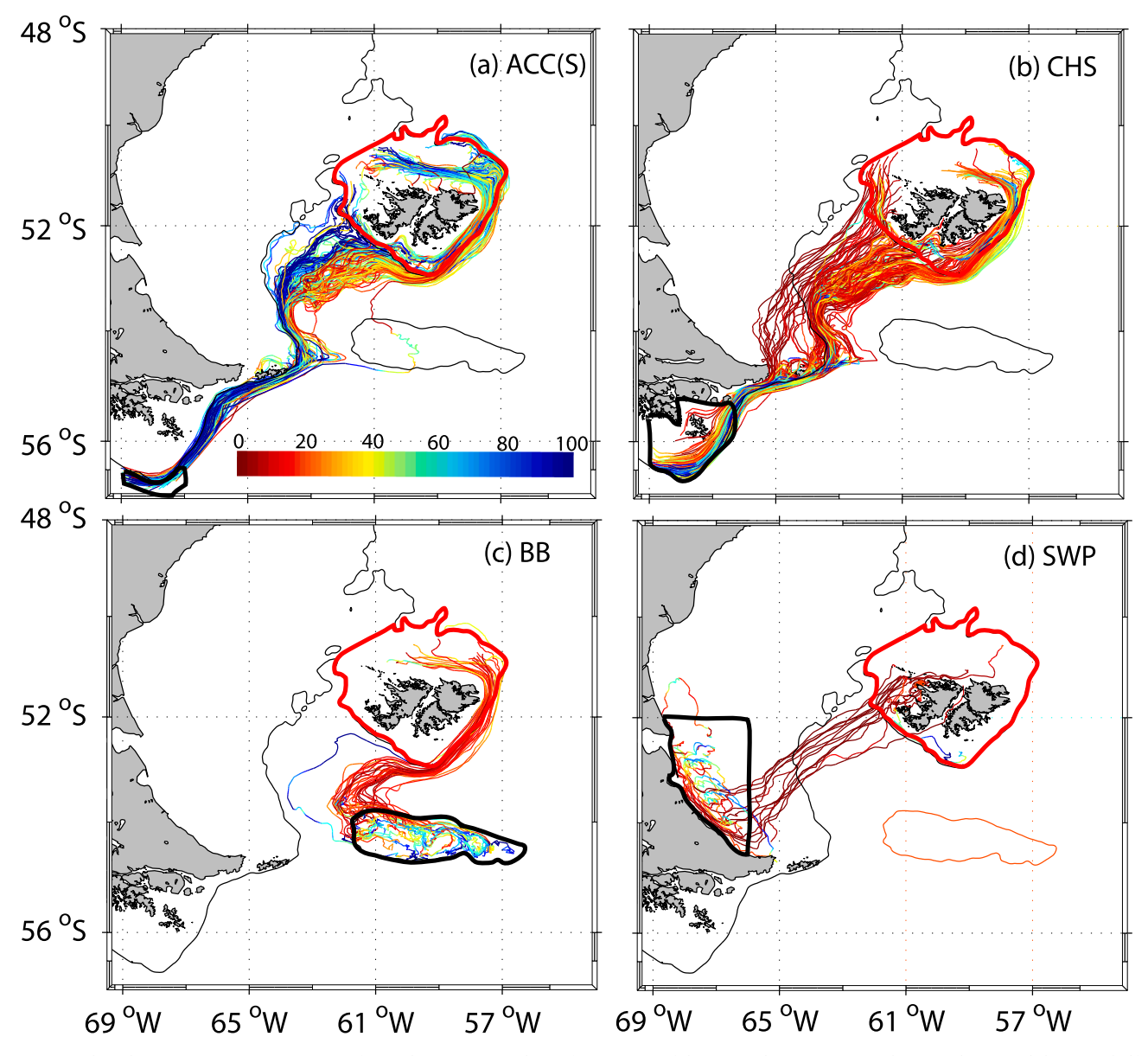


Fig. 8. Forward tracking experiment. Trajectories of particles connecting the surface portion of the ACC polygon [ACC(S)], the CHS, the BB and the SWP shelf with the MIS (red thick line). Particles were released inside the polygons (black thick lines) in September 1st. Trajectories are drawn at the time after release where most particles arrive at the MIS [150 days for ACC(S), CHS and BB and 320 days for SWP]. Colours indicate particle's depth. Only 10% of the trajectories are shown. (For interpretation of the references to color in this figure legend, the reader is referred to the web version of this article.)

year of the CTRL integration. To avoid overlap each of these estimates are made in separate model runs. Thus, for example, in one experiment we release 45,000 particles during January and integrate the model for an entire year. The same procedure is repeated for all the other months. Thus, at the end of these twelve experiments we can estimate residence times for each month of the year. Initially, particles are uniformly distributed between 5 m and the bottom. To evaluate depth dependence, particles are divided in a surface (0–50 m) and a deep (50 m–bottom) group, with membership dictated by their initial position. Each group includes an approximately equal number of particles. The overall residence time (all particles) is characterized by a minimum during fall (70 days) and a maximum during summer and winter (90 days; Fig. 9a). We observe similar seasonal variations for particles released in the surface and deep layers, which are, with the exception of winter, shorter in the surface layer. Minimum/maximum residence times are approximately 45/90 days in the surface layer and 90/130 days in the deep layer. These seasonal variations are driven by changes in stratification and wind forcing. During summer, most particles leaving the MIS originate in the

surface layer and therefore have smaller residence times. Vertical motion of particles in the deep layer are restricted by density stratification and therefore have longer residence times (Suppl. Fig. S2, top panel). Winter convection forces particles towards the surface where they are expelled from the MIS (Suppl. Fig. S2, bottom panel). Winter convection increases the residence time of particles in the surface layer, thus decreasing the residence times in the deep layer. By the end of winter, however, residence times in both layers are similar. During fall and spring, weak stratification allows the residence time to be controlled by the wind intensity over the surface layer, which is stronger in fall and weaker in spring.

A geographic census of the number of particles crossing the 200 m isobath 90 days after their release reveals seasonal differences in detrainment locations. The number of particles leaving the MIS during summer is similar to that leaving during winter, thus reflecting the similar residence times reported above (cf. Fig. 9b and c). During summer the preferential detrainment site from the MIS polygon is the northwestern region and, to a lesser extent, the northeastern portion of

120

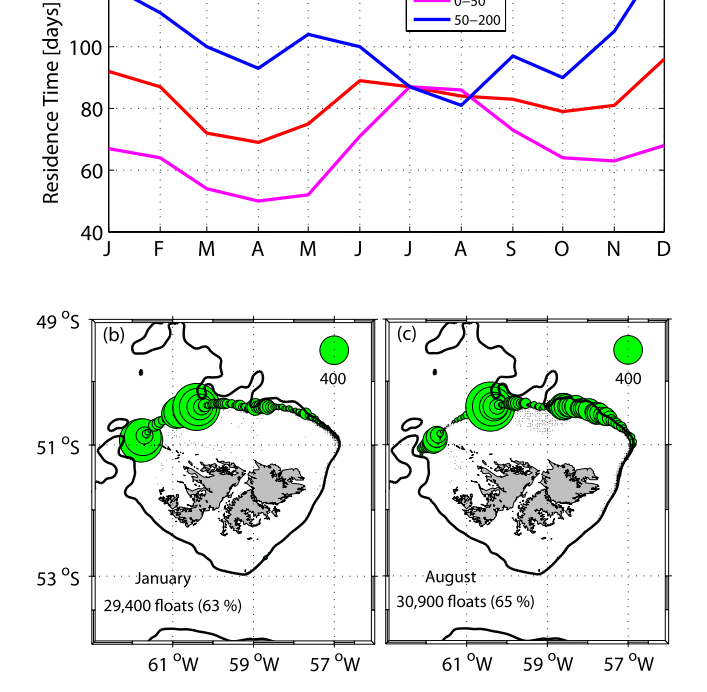
Table 2

(a) Percentage of particles released from selected locations (indicated in Fig. 8) and reaching the MIS after one year. U stands for the upper portion of the ACC polygon (z < 200 m), L is for the remaining lower portion of the water column. (b) percentage of particles released from the MIS and reaching the Patagonian shelfbreak front (PSB) after 180 days. Inshore indicates the PSB polygon located between the 100 and 200 m isobaths (Fig. 10b), Offshore is for polygon located between 200 and 1000 m isobaths (Fig. 10a). Results in (a) and (b) also discriminate those particles arriving at the surface portion of the water column (SUR, 0-50 m) and the deep portion (BOT, 50-bottom); TOT = SUR + BOT. Peak indicates the elapsed time from release (in days) of maximum arrival of particles.

(a) SOUR	CES															
Number of	f Particles ((% wrt the	initial numl	ber) reachi	ng MIS afte	er 1 Year (I	nitial num	ber release	d at each p	oolygon =	14,000)					
	Summer (DEC)				Autumm (MAR)				Winter (JUN)				Spring (SEP)			
	SUR	BOT	TOT	peak	SUR	BOT	TOT	peak	SUR	BOT	TOT	peak	SUR	BOT	TOT	peak
ACC(U)	7.0	29.7	36.7	145	17.8	27.3	45.1	105	16.4	38.2	54.6	159	15.6	20.6	36.2	137
ACC(L)	0.6	8.5	9.10	162	4.9	15	19.9	180	5.2	15.4	20.6	173	4.7	6.0	10.7	140
CHS	8.6	12.9	21.5	162	18.6	10.1	28.7	110	18.5	34.4	52.9	159	25.5	17.4	42.9	90
BB	10.6	4.1	14.7	113	5.3	10.2	15.5	133	1.2	0.3	1.5	238	6.3	1.7	8.00	160
SWP	19.9	0.2	20.1	312	15.6	1.3	16.9	216	21.9	2.1	24	133	11.0	1.0	12	316

Number o	f Particles (% wrt the i	initial num	ber) reachi	ng PSB afte	er 180 day	s (Initial nu	umber relea	ased at MIS	S = 45,000)				
_	Summer (DEC)					m (MAR)			Winter	(JUN)	Spring (SEP)				
	SUR	ВОТ	TOT	peak	SUR	BOT	TOT	peak	SUR	BOT	TOT	peak	SUR	BOT	TOT

	Summer (DEC)				Autumi	Autumm (MAR)				(JUN)			Spring (SEP)				
	SUR	BOT	TOT	peak	SUR	BOT	TOT	peak	SUR	BOT	TOT	peak	SUR	BOT	TOT	peak	
Inshore	15.3	9.7	25	139	10.7	7.2	17.9	120	16.8	7.2	24.0	180	18.2	10.5	28.7	180	
Offshore	17.2	4.7	21.9	54	25.9	3.7	29.6	68	28.7	3.8	32.5	81	18.1	8.1	26.2	73	



0-200

0-50

Fig. 9. (a) Residence time and geographical census of detrainment sites during January (b) and August (c). Residence times are defined as the time it takes to evacuate 63% of the floats (e-folding time) from the MIS. Release depths: 0-50 m (magenta line), 50-bottom (dark blue line), and 0-bottom (200 m red line). Radii of circles in (b) and (c) are proportional to the number of floats leaving the MIS polygon at that location. 45,000 floats are released on top of the MIS at the beginning of each month. (For interpretation of the references to color in this figure legend, the reader is referred to the web version of this article.)

the shelfbreak (Fig. 9b). There is almost no detrainment at the southern portion of the MIS. During late winter, strengthening of the northward flow in the northeastern portion of the shelf increases the outflow intensity along the northeastern shelfbreak (Fig. 4b and Fig. 9c).

To characterize the link between the MIS and the Patagonian shelfbreak front we compute the spatial distribution (average horizontal density) of particles released over the MIS during September (late winter), and the percentage of those particles reaching two shelfbreak front polygons extending from 44°S to 46°S. One covers the inshore portion of the shelfbreak front (100-200 m isobaths) and the other the offshore portion (200-1000 m isobaths; Table 2b and Fig. 10). We distinguish two destination layers within these polygons, the surface layer (z < 50 m) and the deep layer (z > 50 m). Our analysis indicates that there is a significant connection between the waters of the MIS and those of the Patagonian shelfbreak front; on annual average approximately 25% of the particles released over the MIS reach both portions of the shelfbreak front, mostly (15%) in the surface layer (z < 50 m). This percentage slightly increases for the offshore portion (22%). Fewer particles arrive to the deep layer (z > 50 m), and even fewer (<1%) reach depths below 200 m. The percentage of particles reaching the surface layer of the shelfbreak polygons remain stable throughout the year but it is marginally larger for the inshore region during spring and summer and for the offshore regions during fall and winter (Table 2b). The arrival time to both regions, however, is very different. Most particles reach the offshore portion after a relatively short average transit time of 69 days because they are driven by the rapid flow of the Malvinas Current (Fig. 10a). Particles reaching the inshore portion have a longer average transit time of 154 days. The particles distribution shows an almost continuous high-density strip along the 200 m isobath (Fig. 10). This strip is similar to the high chlorophyll-a plumes that are frequently seen in satellite color imagery (Fig. 1a), thus suggesting that advection of nutrient-rich waters from the MIS might contribute to the fertilization of the Patagonia shelfbreak front.

3.5. Obduction mechanisms

The large chlorophyll-a blooms surrounding the MIS (Fig. 11f) suggest a vigorous entrainment of nutrient rich waters from its deep layers. In what follows we will refer to these entrainments, which are not driven by any single dynamical mechanism (i.e., upwelling or mixing), as obduction. Obduction processes are characterized with the analysis of passive tracer releases. The time evolution of these tracers is controlled by an online integration of an advection/diffusion equation similar to that used for temperature and salinity. To characterize the obduction of slope waters (z > 200 m) we inject a tracer in the deep-ocean region surrounding the southern portion of the MIS. The tracer is continuously released inside the hatched region shown in Fig. 11a, which is limited by the 200 m and 400 m isobaths, and injected below 200 m; thus any

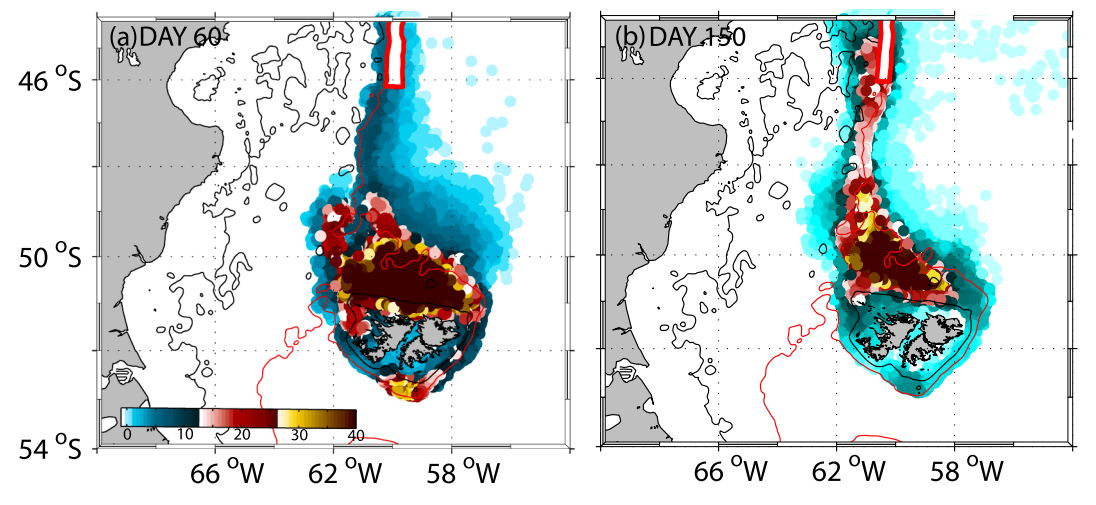


Fig. 10. Connection with the Patagonian shelfbreak-front (PSB). Float concentration (scatter plot) at the surface of particles released over the MIS in September. (a) Particles connecting with the oshore portion of the PSB 60 days after release. (b) particles connecting with the inshore portion of the PSB 150 days after release. The onshore and inshore portions of the PSB are indicated by white rectangles. The black and red lines indicate the 100 m and 200 m isobaths respectively. (For interpretation of the references to color in this figure legend, the reader is referred to the web version of this article.)

tracer signature above 200 m indicates obduction. A source term kept the tracers at an initial concentration Co = 100 in the release areas at all time. Tracer release began December 1 and continues during a threeyear period. The slope tracer first surfaces in the southwestern region (near the 100 m isobath) at day 150, (Fig. 11a), after which it spreads along the isobaths, reaching its maximum surface concentration at the end of the austral winter (Fig. 11b-c). Tracer distribution in mid-spring is characterized by two well-defined plumes wrapping the 100 m isobath with a relatively low concentration between plumes (Fig. 11d). There is a striking similarity between tracer plumes and a SeaWifs color image taken at the beginning of December. Note, in particular, the plume intruding into the northwest corner of the MIS (Fig. 11f). Surface tracer concentration decays during late spring and summer, when the core of the surface plume is located in the lee of the islands and confined to the shelf region (Fig. 11e). During this season obduction is largely restricted to shallow, tidally controlled regions.

To identify the dynamical mechanisms contributing to tracer obduction, we analyze the tracer balance equation. If \mathcal{C} is tracer concentration at each model grid point then its evolution over time obeys the equation,

$$\frac{\partial C}{\partial t} = -u \frac{\partial C}{\partial x} - v \frac{\partial C}{\partial y} - w \frac{\partial C}{\partial z} + \frac{\partial}{\partial z} \left(k_z \frac{\partial C}{\partial z} \right) \tag{1}$$

where *u*, *v* and *w* are the two horizontal and vertical components of the velocity field and k_z is the vertical mixing coefficient. In what follows, the terms of (1) will be called (from left to right) TEND, ADV_H (second and third terms), ADVz and MIXz. To characterize the obduction process we first evaluate the tracer balance at a mid-level point (100 m) of Station A, which is the main shelfbreak obduction region (Fig. 12). The analysis focuses on the first ten days of the experiment (using averages over two M2 periods). Obduction at Station A reflects a balance between the entrainment driven by vertical mixing (MIXz) and the detrainment associated with downwelling (ADVz) and horizontal advection (ADV_H) (Fig. 12). Downwelling, however, is only important during the first couple of days, after which the tracer distribution reflects a balance between what is brought to the surface by (tidal) vertical mixing and what is transported offsite by local currents. Additional stations to the NW and SE of station A (following the 200 m isobath) were also selected to analyse the tracer balance. In those cases the balance highlights the effect of horizontal and vertical advection, with vertical mixing playing a minor role.

To characterize the seasonal evolution of the tracer balance over the

entire MIS we horizontally and vertically average the terms of (1) in a surface layer (0-50 m) and a deep layer (50 m-bottom) (see Fig. 7c). Fig. 13 (top panels), therefore, indicates the volume-averaged tracer concentration in each layer. Tracer development in the deep layerwhere obduction begins-exhibits three well-defined phases: a near steady increase during summer and fall, a rapid growth during winter and an equally rapid decay during spring (Fig. 13a). The tracer balance shows that, in the deep layer, the nearly constant value of tracer concentration during the first quarter of the year (January to May) reflects a balance between tracer horizontally advected from the surrounding deep ocean region (ADV_H) and upwelled into the surface layer (ADV_Z) (Fig. 13b). Convective overturning during winter led to a steep growth of tracer concentration. During this season the increase in tracer concentration is not only associated with localized overturning (MIXz) but also with horizontal transport of tracer obducted in the surrounding region. During spring, the combined effects of vertical mixing and advection deplete the tracer of the deep layer (Fig. 13b). The three phases in tracer evolution, which are created by seasonal changes in density stratification, are more defined in the surface layer (Fig. 13c). There, the growth of the tracer concentration during summer is more restricted because of the stronger stratification. Thus, during this season, horizontal advection leads to a rapid decrease of the tracer concentration in the surface layer. Winter convection and spring re-stratification controls the further evolution of the tracer in this layer. During spring, the system is reset and the excess tracer of the surface layer is evacuated in the Ekman layer (Fig. 13d).

Tracer releases in the process-oriented experiments (Table 1) allows identification of the obduction drivers. The evolution curves show that tracer obduction is largely driven by the synergetic interaction of tides and wind forcing (Fig. 14). Water depth limits obduction by tidal mixing; thus, in deep regions—where tides are unable to entrain the tracer into the surface layer—the contribution of wind forcing provided the energy for further uplift of the tracer. This interaction is illustrated in Fig. 15, which shows the surface plume generated by the processoriented experiments. In these experiments the tracer is released over the MIS below 50 m and between the 50 m and 100 m isobaths. Tides and winds uplift the tracer to the surface but in different regions of the shelf. In experiment ACC&TIDES, for example, the tracer is transported from its source to shallower regions, where it can be uplifted by the local tides, thus generating a surface plume bounded by the 50 m isobath (Fig. 15b). In experiment ACC&WINDS, the tracer plume is confined to the western coast of the Gran Malvina (Fig. 15c). Here, the tracer injected into the bottom layers of the shelf can only be uplifted in the

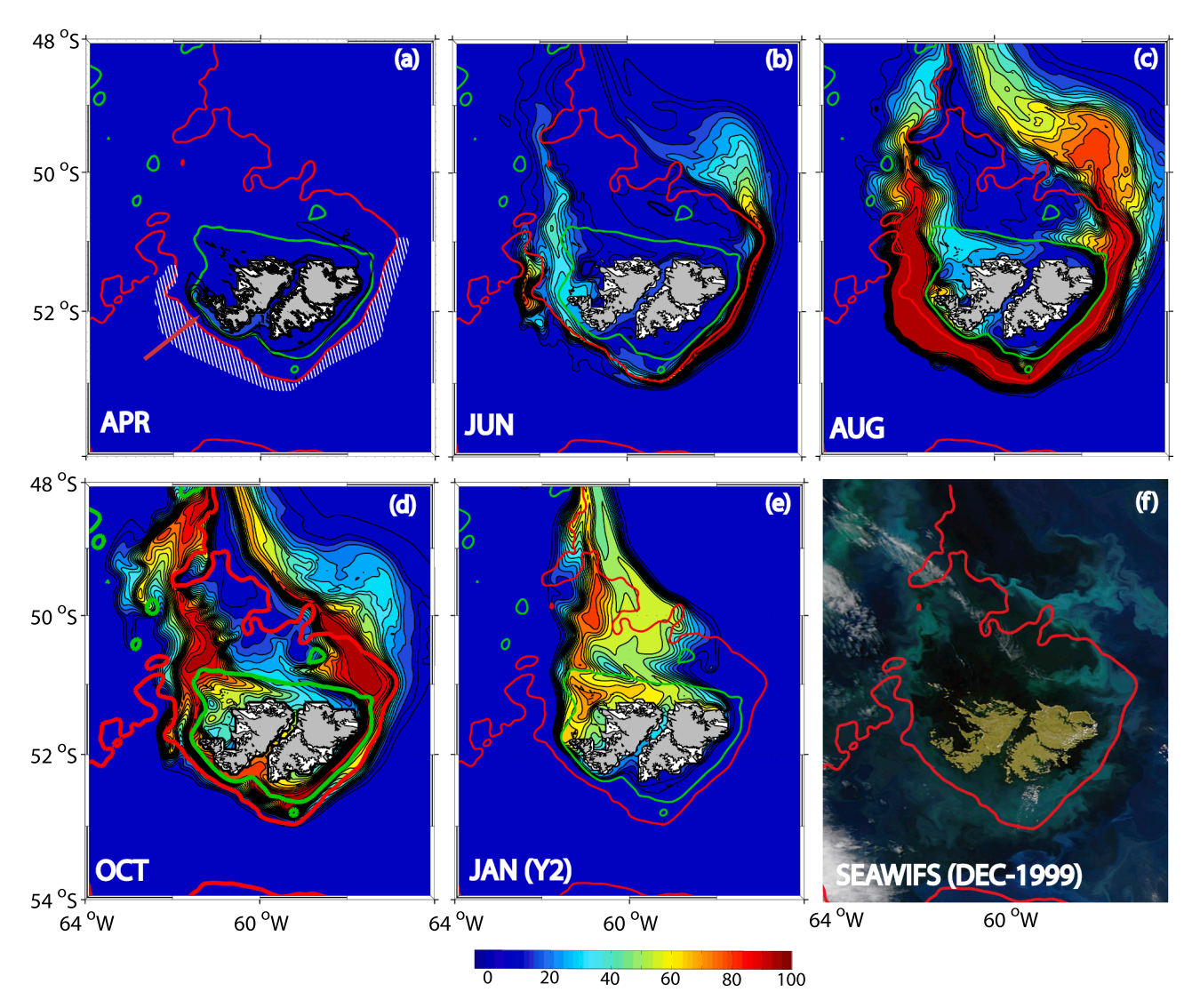


Fig. 11. Time evolution of a passive tracer. The tracer was released below 200 m and between the 200 m and 400 m isobaths (hatched area in panel (a)) at the beginning of December. (a) to (e) surface tracer concentration (30-day averages) at different months. Panel (f) is a SeaWifs color image from December 13, 1999. The green and red lines indicate the 100 m and 200 m isobaths respectively. The red arrow in (a) shows the region where the tracer first appears at the surface. (For interpretation of the references to color in this figure legend, the reader is referred to the web version of this article.)

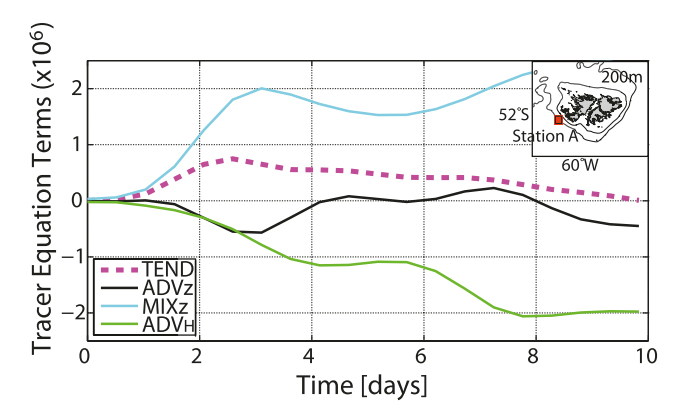


Fig. 12. Tracer evolution over the slope region. Time evolution of the different terms of the tracer balance equation at 100 m depth at station A (inset).

wind-driven upwelling region of the western (Fig. 6b) and northwestern coasts (Fig. 5b). Experiment ACC_ONLY shows no surface tracer development (Fig. 15d). Experiment CTRL shows that the combined action of

tides and winds generated a stronger plume than any of the drivers alone (Fig. 15a). Here, tides do most of the uplifting while winds reinforce the obduction and also contribute to the horizontal spreading of the plume. Note also the similarity between Fig. 15a (CTRL average tracer concentration) and Fig. 1b (average satellite chlorophyll-a concentration).

This article is largely focused on low-frequency phenomena. Obduction, however, is a high-frequency process and although our model configuration includes tidal forcing it only uses monthly averaged wind forcing. It seems natural then, to wonder how obduction would be affected by the inclusion of higher frequency wind forcing. To investigate these matters we run an additional suite of experiments forced with 3-day average winds instead of monthly mean winds. These experiments, which will be discussed in some detail in an upcoming article, indicate that with the use of high-frequency winds there is only moderate strengthening of the obduction of passive tracers because the impact of local wind forcing is modulated by the tides.

4. Summary and discussion

The MIS circulation is dominated by two currents drawn from the northernmost branch of the ACC. These currents wrap around the sides

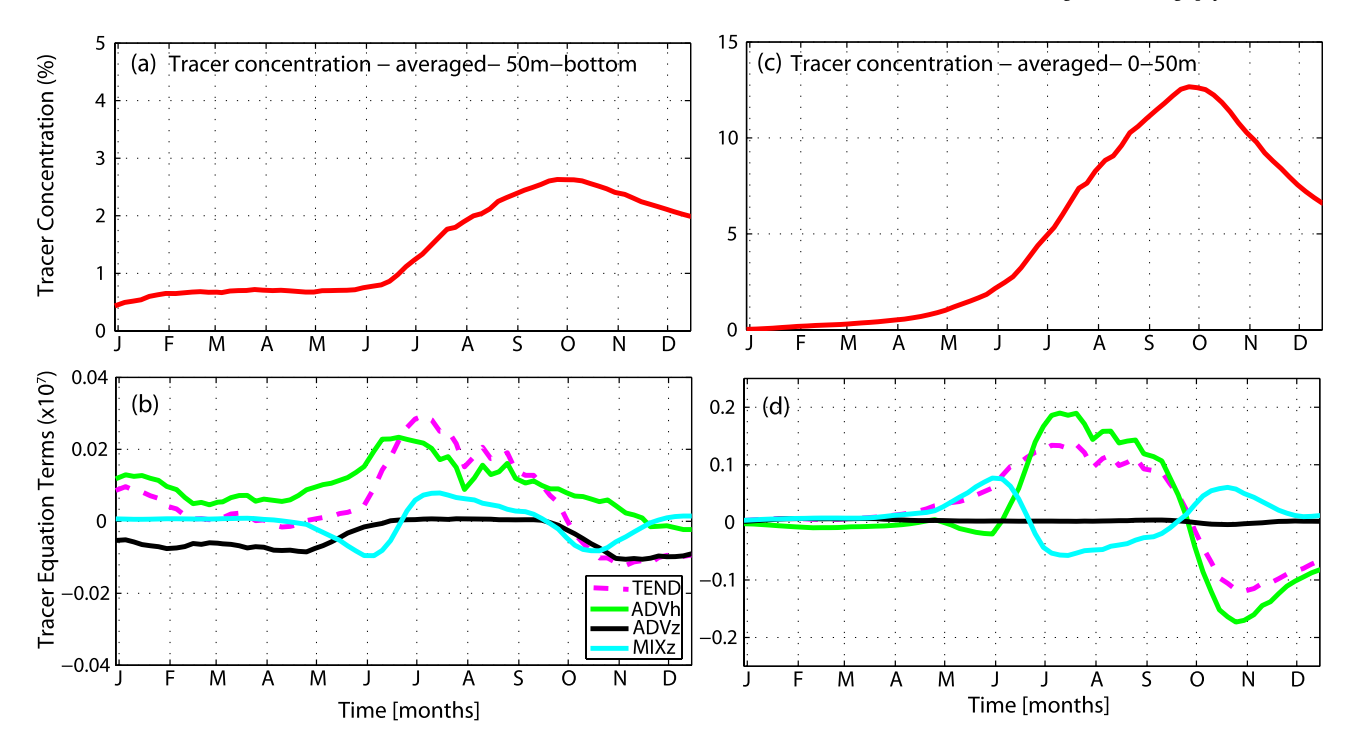


Fig. 13. Tracer evolution over the MIS polygon (see Fig. 3a). Top panels show the time evolution of the volume-averaged tracer concentration. Tracer is injected between the 200 m and 400 m isobaths and below 200 m (Fig. 11a): (a) 50 m to bottom and (c) 0–50 m (see Fig. 7c). Bottom panels show the time evolution of the different terms of the tracer balance equation: (b) 50 m to bottom and (d) 0–50 m.

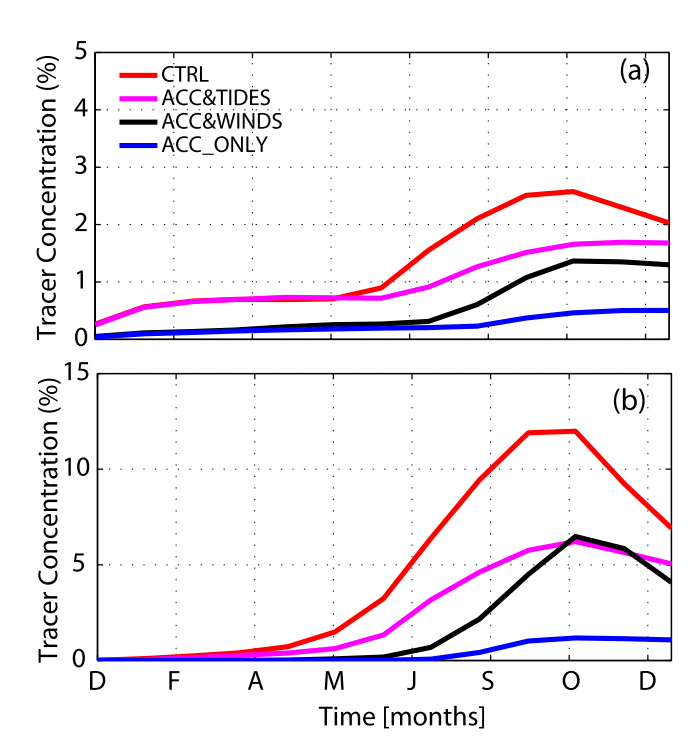


Fig. 14. Time evolution of the volume-averaged tracer concentration over the MIS for different sensitivity experiments (Table 1). Tracer is injected between the 200 m and 400 m isobaths and below 200 m (Fig. 11a): (a) 50 m-bottom, and (b) 0–50 m.

of the islands thus developing an anticyclonic circulation pattern that intensifies during summer and weakens during winter. The blocking effect of the islands generates an eastward current in the northern portion of the MIS along the coast and a westward current farther offshore, which flows in the upwind direction. The largest inflows of

deep-ocean waters onto the shelf are observed at the place where the ACC, steered by abrupt changes of the bottom topography, collides with the MIS. Deep-ocean entrainments are sharply reduced farther downstream, although they are still significant. Shelf water outflows are larger in the northwestern section connecting the MIS to the Patagonian Shelf and diminish towards the east where they are entrained into the Malvinas Current.

Circulation patterns in the offshore region are very similar to those based on hydographic data (Piola and Gordon, 1989), current meter data and satellite altimetry (Frey et al, 2021) and model reanalysis (Artana et al., 2021). There is insufficient observational data, however, to validate the shelf circulation patterns. Prior analyses, nevertheless, show that the model compare favorably with different types of satellite data and tide gauge records (Combes and Matano, 2014a; 2018; 2019; Matano et al., 2014; 2019; Palma et al., 2020). Further assessment of the model results is hampered by the dearth of observational data. Based on hydrographic observations, however, Arkhipkin et al. (2010) proposed a schematic of circulation pattern in the western sector of the MIS that is qualitatively similar to the circulation patterns inferred from our model results (Fig. 4a). Cross-sections of temperature data collected during austral summer in the southern portion of the MIS (Arkhipkin et al., 2004) indicate a well-mixed coastal region, a strong bottom boundary layer front near the 50 m isobath and cold AAIW waters temperatures below, features that are well reproduced by the model (Fig. 5b).

Particle tracking experiments indicate that the northern portion of the Drake Passage is the largest water mass source to the MIS. During summer, more particles reach the deep layer while in spring more particles reach the surface layer. The shelf portion of this region—the Cape Horn shelf—largely feeds MIS surface waters, except in winter where the contribution is larger in the deep layer. There is a relatively weak connection between the Burdwood Bank and the MIS, which strengthens during the summer and in the surface layer (see also Matano et al., 2019). In agreement with hydrographic data (Arkhipkin et al., 2010) passive tracers indicate that the place where the ACC collides with the MIS is the main shelfbreak obduction region. After its first appearance in the surface layer the tracer spreads along the southwestern rim, reaching

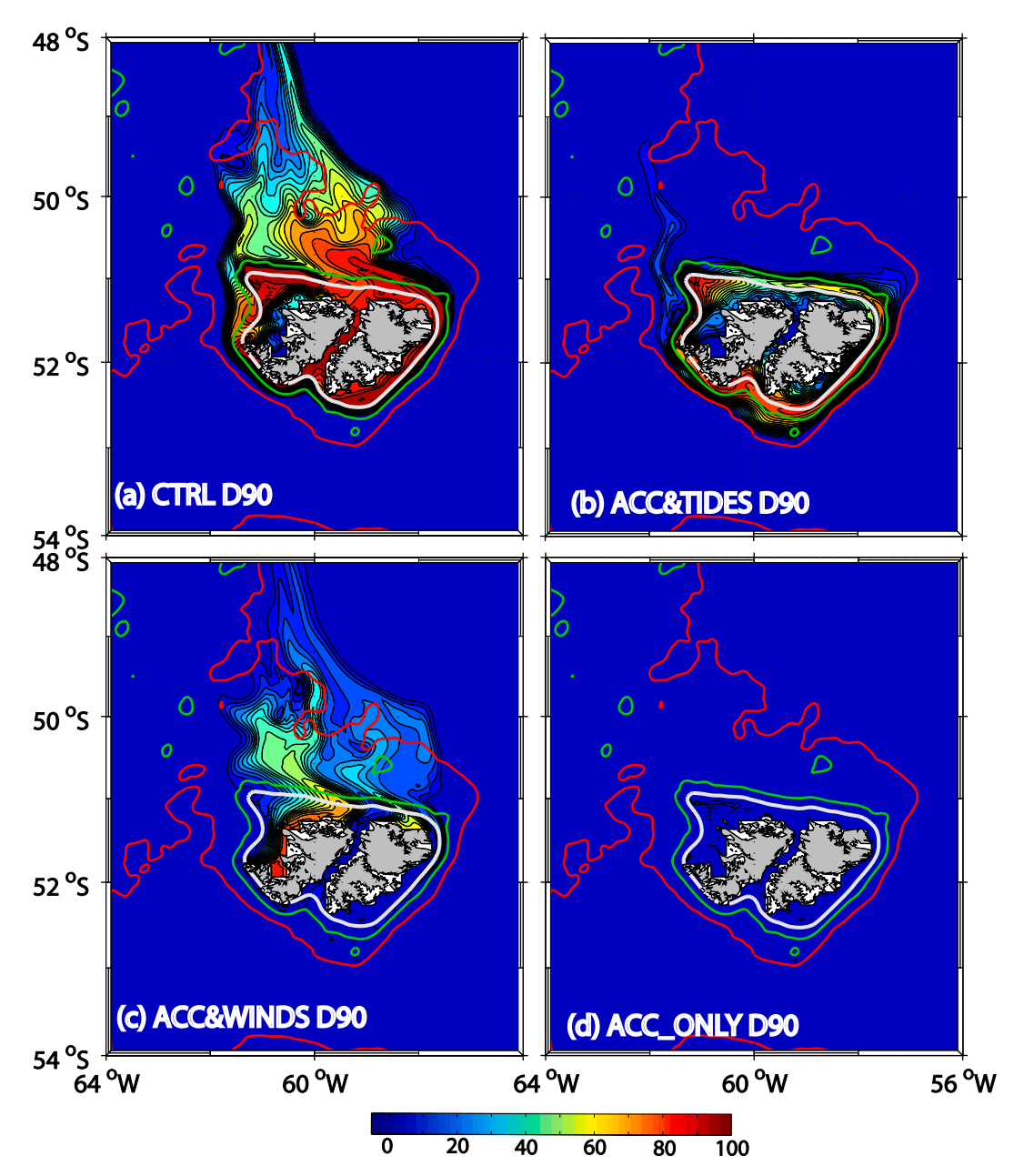


Fig. 15. Time evolution of a passive tracer. Tracer was released over the MIS below 50 m and between the 100 m and 50 m isobaths. (a) to (d) concentration at the surface and 90 days after release (30-day averages) under different sensitivity experiments (see Table 1). The red, green and white lines are the 200, 100 and 50 m isobaths respectively. (For interpretation of the references to color in this figure legend, the reader is referred to the web version of this article.)

its maximum surface concentration at the end of austral winter fueled by winter convection. The surface tracer concentration along the rim decays during the spring with the onset of vertical stratification. The tracer that remains on the shelf is subsequently entrained in the surface layer driven by the synergetic interaction of tides and wind forcing. There tides can bring the tracer close to the surface layer where the wind forcing does the rest of the uplifting. Consequently, at the beginning of the summer the core of the surface plume is located on the lee of the islands and confined to the shelf region.

To further characterize the connectivity of the MIS we analyzed the pathways of neutrally buoyant particles released over the shelf. This connectivity pattern is not only relevant to our understanding of the fertilization processes contributing to the remarkable high productivity of Patagonia's shelfbreak region (Romero et al., 2006), but also to the potential detrimental impact of environmental disasters on this fragile marine ecosystem. Particle tracking experiments show that there is an

important contribution of MIS waters to the surface layer of the Patagonian shelfbreak front. This contribution remains stable yearlong and is marginally larger for the inshore portion (100–200 m isobaths) during spring and summer ($\sim 16\%$ of the released particles) and for the offshore sector (200–1000 m isobaths) during fall and winter ($\sim 27\%$). The spatial distribution shows an almost continuous strip of high particle density from the lee of the islands towards the shelfbreak roughly following the outer Patagonian Shelf and shelfbreak. Chlorophyll-a plumes similar to those generated by this simulation are frequently seen in satellite color imagery (Fig. 1a).

The MIS is a potentially important oil and gas reservoir (Zabanbark, 2011). Oil-related activities are still incipient but their anticipated increments will significantly increase the risk of oil spills. The question, therefore, is how such spills might affect the downstream region. Modelling oil dispersion can be quite complex owing to numerous chemical factors that impact its buoyancy (Reed et al., 1999). However,

experiments with neutrally buoyant particles can reveal information about the dominant transport direction and time scales that would be expected in the event of an oil spill. In this respect, our calculation suggests that this kind of event would be extremely detrimental to the Patagonian shelf break ecosystem, particularly its most productive inshore portion (Fig. 10).

Declaration of Competing Interest

The authors declare that they have no known competing financial interests or personal relationships that could have appeared to influence the work reported in this paper.

Acknowledgements

E.D. Palma acknowledges financial support from Agencia Nacional de Promoción Científica y Tecnológica (grant PICT16-0557) and Universidad Nacional del Sur (grant 24F079), Argentina. R. Matano and V. Combes acknowledge the financial support of NASA support through grants 80NSSC21K0559 and NNX17AH60G and the National Science Foundation grant OCE-1830856. MODIS data (Fig. 1) and SeaWifs data (Fig. 11f) are from NASA Ocean Color Group (https://oceancolor.gsfc.nasa.gov). We thank Alberto Piola for his helpful comments. The paper benefited substantially from suggestions given by two anonymous reviewers.

Appendix A. Supplementary material

Supplementary data to this article can be found online at https://doi.org/10.1016/j.pocean.2021.102666.

References.

- Agnew, D.J., Hill, S., Beddington, J.R., 2000. Predicting the recruitment strength of an annual squid stock: Loligo gahi around the Falkland Islands. Can. J. Fish. Aquat. Sci. 57 (12), 2479–2487.
- Amante, C., Eakins, B.W., 2009. ETOPO1 1 arc-minute global relief model: procedures, data sources and analysis. National Geophysical Data Center, NOAA, Boulder Colorado.
- Antonov, J. I., D. Seidov, T. P. Boyer, R. A. Locarnini, A. V. Mishonov, H. E. Garcia, O. K. Baranova, M. M. Zweng, and D. R. Johnson, (2010). World Ocean Atlas 2009, Volume 2: Salinity. S. Levitus, Ed. NOAA Atlas NESDIS 69, U.S. Government Printing Office, Washington, D.C., 184 pp.
- Arkhipkin, A.I., Middleton, D.A.J., Sirota, A.M., Grzebielec, R., 2004. The effect of Falkland Current inflows on offshore ontogenetic migrations of the squid Loligo gahi on the southern shelf of the Falkland Islands. Estuar. Coast. Shelf Sci. 60 (1), 11–22.
- Arkhipkin, A., Brickle, P., Laptikhovsky, V., 2010. The use of island water dynamics by spawning red cod, Salilota australis (Pisces: Moridae) on the Patagonian Shelf (Southwest Atlantic). Fish. Res. 105 (3), 156–162.
- Artana, C., Provost, C., Poli, L., Ferrari, R., Lellouche, J.-M., 2021. Revisiting the Malvinas Current upper circulation and water masses using high-resolution ocean reanalysis. J. Geophys. Res. Oceans 126 e2021JC01721.
- Ashford, J.R., Fach, B.A., Arkhipkin, A.I., Jones, C.M., 2012. Testing early life connectivity supplying a marine fishery around the Falkland Islands. Fish. Res. 121-122, 144-152.
- Barnier, B., 1998. Forcing the ocean. In: Chassingnet, E.P., Verron, J. (Eds.), Ocean Modelling and Parameterization. Kluwer Academic Publishers, The Netherlands, pp. 45–80.
- Baylis, A.M.M., Tierney, M., Orben, R.A., Warwick-Evans, V., Wakefield, E., Grecian, W. J., Trathan, P., Reisinger, R., Ratcliffe, N., Croxall, J., Campioni, L., Catry, P., Crofts, S., Boersma, P.D., Galimberti, F., Granadeiro, J.P., Handley, J., Hayes, S., Hedd, A., Masello, J.F., Montevecchi, W.A., Pütz, K., Quillfeldt, P., Rebstock, G.A., Sanvito, S., Staniland, I.J., Brickle, P., 2019. Important at-sea areas of colonial breeding marine predators on the southern Patagonian Shelf. Sci. Rep. 9 (1) https://doi.org/10.1038/s41598-019-44695-1.
- Boltovskoy, D. (Ed.), 2000. South Atlantic zooplankton. Backhuys Publishers, Leiden. Combes, V., Matano, R.P., 2014a. A two-way nested simulation of the oceanic circulation in the Southwestern Atlantic. J. Geophys. Res. Oceans 119 (2), 731–756.
- Combes, V., Matano, R.P., 2014b. Trends in the Brazil/Malvinas confluence region. Geophys. Res. Lett. 41 (24), 8971–8977.
- Combes, V., Matano, R.P., 2018. The Patagonian shelf circulation: Drivers and variability. Prog. Oceanogr. 167, 24–43. https://doi.org/10.1002/2013JC009498.
- Combes, V., Matano, R.P., 2019. On the origins of the low-frequency sea surface height variability of the Patagonia shelf region. Ocean Model. 142, 101454. https://doi.org/10.1016/j.ocemod.2019.101454.

- Da Silva, A. M., C. C. Young, and S. Levitus (1994). Atlas of Surface Marine Data 1994, vol. 1, Algorithms and Procedures, NOAA Atlas NESDIS 8, 83 pp., U. S. Dep. of Commer., NOAA, NESDIS, Washington, D.C.
- Egbert, G.D., Bennett, A.F., Foreman, M.G.G., 1994. Topex/Poseidon tides estimated using a global inverse model. J. Geophy. Res Oceans 99 (C12), 24821. https://doi. org/10.1029/94JC01894.
- Fetter, A.F.H., Matano, R.P., 2008. On the origins of the variability of the Malvinas Current in a global, eddy-permitting numerical simulation. J. Geophys. Res. Oceans 113 (C11). https://doi.org/10.1029/2008JC004875.
- Frey, D.I., Piola, A.R., Krechik, V.A., Fofanov, D.V., Morozo, E.G., Silvestrova, K.P., et al., 2021. Direct measurements of the Malvinas Current velocity structure. J. Geophys. Res Oceans 126 e2020JC01672.
- Glorioso, P.D., Flather, R.A., 1997. The Patagonian Shelf tides. Prog. Oceanog. 40, 263 283.
- Guerrero, R.A., Baldoni, A., Benavides, H., 1999. Oceanographic conditions at the southern end of the Argentine continental slope. INIDEP Doc. Cient. 5, 7–22. Contribution 1083.
- Guihou, K., Piola, A.R., Palma, E.D., Chidichimo, M.P., 2020. Dynamical connections between large marine ecosystems of austral South America based on numerical simulations. Ocean Sci. 16, 271–290.
- Harte. E.M., 2020. Testing the connectivity of Dissostichus eleginoides (Patagonian toothfish) between the Pacific coast of southern Chile and the Patagonian shelf in the southwest Atlantic, MsScience Thesis, University of Otago Dunedin, New Zealand.
- Jones, D.J.R., McCarthy, D.J., Dodd, T.J.H., 2019. Tectonostratigraphy and the petroleum systems in the Northern sector of the North Falkland Basin, South Atlantic. Mar. Pet. Geol. 103, 150–162.
- Large, W., McWilliams, J., Doney, S., 1994. Oceanic vertical mixing—a review and a model with a nonlocal boundary-layer parameterization. Rev. Geophys. 32 (4), 363–403.
- Lee, B., Brewin, P.E., Brickle, P., Randhawa, H., 2018. Use of otolith shape to inform stock structure in Patagonian toothfish (Dissostichus eleginoides) in the southwestern Atlantic. Mar. Freshw. Res. 69 (8), 1238–1247.
- Locarnini, R. A., A. V. Mishonov, J. I. Antonov, T. P. Boyer, H. E. Garcia, O. K. Baranova,
 M. M. Zweng, and D. R. Johnson, (2010). World Ocean Atlas 2009, Volume 1:
 Temperature. S. Levitus, Ed. NOAA Atlas NESDIS 68, U.S. Government Printing
 Office, Washington, D.C., 184 pp.
- Marchesiello, P., McWilliams, J.C., Shchepetkin, A., 2001. Open boundary conditions for long-term integration of regional oceanic models. Ocean Modell 3 (1-2), 1–20.
- Marrari, M., Piola, A.R., Valla, D., 2017. Variability and 20-Year trends in satellite-derived surface chlorophyll concentrations in large marine ecosystems around south and western central America. Front. Mar. Sci. 4, 372. https://doi.org/10.3389/fmars.2017.00372.
- Matano, R.P., Palma, E.D., 2008. On the upwelling of downwelling currents. J. Phys. Oceanogr. 38, 2482–2500.
- Matano, R.P., V. Combes, A. R. Piola, R. Guerrero, E. D. Palma, P. T. Strub, C. James, H. Fenco, Y. Chao, Y. and M. Saraceno (2014). The salinity signature of the cross-shelf exchanges in the Southwestern Atlantic Ocean: Numerical simulations. J. Geophys. Res. (Oceans), 119(11), 7949-7968.
- Matano, R.P., Palma, E.D., Combes, V., 2019. The Burdwood Bank Circulation.
 J. Geophys Res. Oceans 124, 6904–6926.
- Miller, Robert N., Matano, Ricardo P., Palma, Elbio D., 2011. Shelfbreak upwelling induced by alongshore currents: analytical and numerical results. J. Fluid Mech. 686, 239–249.
- Painter, Stuart C., Poulton, Alex J., Allen, John T., Pidcock, Rosalind, Balch, William M., 2010. The COPAS'08 expedition to the Patagonian Shelf: Physical and environmental conditions during the 2008 coccolithophore bloom. Cont. Shelf Res. 30 (18), 1907–1923.
- Palma, Elbio D., Matano, Ricardo P., Piola, Alberto R., 2004. A numerical study of the Southwestern Atlantic Shelf circulation: Barotropic response to tidal and wind forcing. J. Geophys. Res. Oceans 109 (C8), n/a-n/a. https://doi.org/10.1029/ 2004JC002315.
- Palma, E.D., Matano, R.P., Piola, A.R., 2008. A numerical study of the Southwestern Atlantic Shelf circulation: stratified ocean response to local and offshore forcing. J. Geophys. Res. Oceans 113, C11010. https://doi.org/10.1029/2007JC004720.
- Palma, Elbio D., Matano, Ricardo P., Tonini, Mariano H., Martos, Patricia, Combes, Vincent, 2020. Dynamical Analysis of the Oceanic Circulation in the Gulf of San Jorge, Argentina. J. Mar. Syst. 203, 103261. https://doi.org/10.1016/j. jmarsys.2019.103261.
- Piola, Alberto R., Gordon, Arnold L., 1989. Intermediate waters in the southwest South Atlantic. Deep Sea Res. Part A. 36 (1), 1–16.
- Randhawa, H.S., Lee, B., Brickle, P., Reid, M.R., Arkhipkin, A.I., 2020. Oceanographic cues determine the recruitment demography of toothfish Dissostichus eleginoides on the Patagonian Shelf: evidence from otolith microchemistry. Manuscript submitted for publication.
- Reed, Mark, Johansen, Øistein, Brandvik, Per Johan, Daling, Per, Lewis, Alun, Fiocco, Robert, Mackay, Don, Prentki, Richard, 1999. Oil spill modeling towards the close of the 20th century: overview of the State of the Art. Spill Sci. Technol. Bull. 5 (1), 3–16.
- Richards, P.C., Hillier, B.V., 2000. Post-drilling analysis of the north Falkland Basin –Part 2: petroleum system and future prospects. J. Petrol. Geol. 23 (3), 273–292.
- Romero, Silvia I., Piola, Alberto R., Charo, Marcela, Garcia, Carlos A. Eiras, 2006. Chlorophyll-a variability off Patagonia based on SeaWiFS data. J. Geophys. Res. 111 (C5) https://doi.org/10.1029/2005JC003244.
- Strub, P.T., James, C., Combes, V., Matano, R.P., Piola, A.R., Palma, E.D., Saraceno, M., Guerrero, R.A., Fenco, H., Etcheverry, L., 2015. Altimeter-derived seasonal

circulation on the southwest Atlantic shelf: 278–438S. J. Geophys. Res. (Oceans)

120, 3391–3418.

Zabanbark, A., 2011. Geological structure and prospect of the oil and gas bearing of the Falkland Islands Region. Oceanology 51 (3), 511–517.

Zyranov, V.N., Severov, D.N., 1979. Water circulation in the Falkland-Patagonian region and its seasonal variability. Oceanology 29, 782–790.